IEEE Access
Multidisciplinary | Rapid Review | Open Access Journal

SPECIAL SECTION ON ADVANCED INFORMATION SENSING AND LEARNING TECHNOLOGIES FOR DATA-CENTRIC SMART HEALTH APPLICATIONS

Received March 21, 2019, accepted April 19, 2019, date of publication April 23, 2019, date of current version May 6, 2019.

Digital Object Identifier 10.1109/ACCESS.2019.2912956

Remote Monitoring of Human Vital Signs Using mm-Wave FMCW Radar

MOSTAFA ALIZADEH[1], (Student Member, IEEE), GEORGE SHAKER[2,3,4], (Senior Member, IEEE), JOÃO CARLOS MARTINS DE ALMEIDA[5], PLINIO PELEGRINI MORITA[6], AND SAFEDDIN SAFAVI-NAEINI[7], (Life Fellow, IEEE)

[1]Electrical and Computer Engineering Department, University of Waterloo, Waterloo, ON N2L 3G1, Canada
[2]Department of Electrical and Computer Engineering, University of Waterloo, Waterloo, ON N2L 3G1, Canada
[3]Department of Mechanical and Mechatronics Engineering, University of Waterloo, Waterloo, ON N2L 3G1, Canada
[4]Research Institute for Aging, Waterloo, ON N2J 0E2, Canada
[5]Biomedical Engineering Department, University of Campinas, Campinas, Brazil
[6]School of Public Health and Health Systems, University of Waterloo, Waterloo, ON N2L 3G1, Canada
[7]Electrical and Computer Engineering Department, University of Waterloo, Waterloo, ON N2L 3G1, Canada

Corresponding author: Mostafa Alizadeh (m5alizad@uwaterloo.ca)

This work was supported by Natural Sciences and Engineering Research Council (NSERC) of Canada and Schlegel Research Institute for Aging (RIA).

ABSTRACT Electromagnetic radars have been shown potentially to be used for remote sensing of biosignals in a more comfortable and easier way than wearable and contact devices. While there is an increasing interest in using radars for health monitoring, their performance has not been tested and reported either in practical scenarios or with acceptable low errors. Therefore, we use a frequency modulated continuous wave (FMCW) radar operating at 77 GHz in a bedroom environment to extract the respiration and heart rates of a patient, who is used to lying down on the bed. Indeed, the proposed signal processing contains advanced phase unwrapping manipulation, which is unique. In addition, the results are compared with a reliable reference sensor. Our results show that the correlations between the reference sensor and the radar estimates are in 94% and 80% for breathing and heart rates, respectively.

INDEX TERMS Breathing rate monitoring, FMCW radar, heart rate monitoring, Hexoskin, mm-wave, non-contact monitoring, phase analysis, remote sensing, vital signs, TI.

I. INTRODUCTION

Monitoring vital signs of a human like heart rate and breathing rate is very critical for saving lives. Individuals might suffer from a disease such as sleep apnea, or their lives have been threatened by a natural disaster. In the former case, there is a need for continuous surveillance of a patient in a room while in the latter case the problem is finding the victims through obstacles like walls. In all of them, it is not possible to attach a device to the subject body to record and analyze their health-related signals. One solution is using radars with the capability of sensing any environment dynamics. The general principle of a typical radar is sending a specific signal then listening to its echo in order to extract environmental features. This idea is not new as it has been used by bats for million years ago (see [1]) in that they use acoustic waves. The acoustic waves could not travel a long distance and they are easily interfered with any mechanical movements and they need a medium for propagation. In contrast, electromagnetic (EM) waves can propagate without any medium and can penetrate through obstacles and do not have the limitations of acoustic waves.

Among popular applications of EM radars, biomedical sensing has gained increasing attention for adopting them in remote sensing of vital signs such as heart rate (HR), breathing rate (BR), blood oxygen density etc. For instance, radars can find HR and BR by detecting the chest wall movement. This is greatly helpful for reducing the number of contact biomedical sensors for monitoring of a patient over a long time. For example, to monitor sleep apnea, in [2] the authors proposed a remote controlling system, which uses a 24 GHz radar.

The authors in [3] also proposed a time-varying filter to reduce noise in order to extract the heart rate with an

The associate editor coordinating the review of this manuscript and approving it for publication was Qingxue Zhang.

impulse radar. Initially the algorithm finds the respiration rate. Then it adopts a time-varying filter after which the derivative of the received signal is taken to increase the signal to noise ratio (SNR) for the estimation of the heart rate. Although this paper considered how to increase SNR for detecting the heart rate, there was no thorough description of the experiment equipment and the setup. Indeed, the accuracy of the reference sensor has not been reported.

As we are interested in using FMCW radar it is important to notice that there is no comprehensive analysis for the Doppler accuracy of FMCW radars. But in [4], authors investigated the range accuracy considering non-idealities in FMCW generation. This is the first paper using direct digital synthesizer (DDS) for artificially adding non-linearities and phase noise to evaluate their effects on the range detection.

In the generation of an FMCW signal a sort of phase randomness appears, which is called phase noise. While it is manifesting itself in the phase, it has impact on the magnitude of the generated signal. In addition, the phase noise degrades the quality of the parameter estimation in any radars particularly FMCW radars. In general, the phase noise effect in the range detection of any radar kind is discussed in [5]. When the echo signal is mixed with the transmitted signal at the receiver, the phase noise autocorrelation becomes a function of transmitted phase noise autocorrelation. This phenomenon is called the *range correlation effect*. In brief, [5] clarifies that the phase noise effect in the range detection of any radar system increases as the range of the subject increases. Fortunately, the phase noise due to the range correlation effect is very low for our case because the subject is very close to the radar located at a few meters distance.

In [6], the authors investigated the main reason for reflecting an EM wave from a body in microwave frequencies. In particular, there are two main reasons: 1) blood perfusion underneath of the skin surface leading to the skin impedance variation, 2) skin/body surface movement. By designing some experiments, they found out the body displacement has a higher influence on reflecting the signal than the impedance change of the skin surface. Their research was conducted in microwave frequencies at which a portion of the wave can penetrate the body. While in mm-wave frequencies, as we consider, the wave is totally reflected off the body surface.

Similarly, in [7], the authors used the FMCW radar for the purpose of the vital sign detection. To choose the start frequency, they tested the FMCW radar at different start frequencies with different bandwidth and different subject position. At the end, they came up with a great conclusion that the radar reliably senses vital signs for many cases, but they chose 9.6 GHz for the purpose of the demonstration and implementation by considering the other factors such as the low interference on the local wireless networks. They analyzed the magnitude and the phase of the received echo signal and they showed that the vital signs detection can be carried out on either phase or magnitude. This result is against the discussion in [8] where the authors illustrated that the magnitude analysis comes with higher order harmonics which degrades the vital sign rate detection robustness, instead they exploited the phase extraction as we will. Furthermore, [7] did not discuss the linear phase trend that is apparent in the captured phase. This behavior seems to be the impact of the hardware non-linearities while they neglected with no more clarification. The linear trend is like a flicker noise, but in the phase domain, and it can affect the vital signs' detection. Although the HR accuracy is reported in [7], BR correct detection rate has not been reported. But in this work, we will investigate both BR and HR and their waveforms experimentally.

A similar phase acquisition using FMCW radar at 80 GHz was presented in [9]. The authors assumed that the distance of the target is known, therefore they did not concentrate on designing an algorithm for finding the targets' range. In addition, the radar was tested in front, back, left, and right sides of the subject when the target was sitting on a chair. This experiment setup cannot be used for a practical clinical purpose when a patient is supposed to laying down on the bed with lots of background clutters. In addition, they did not use phase unwrapping and we will show that is necessary in mm-wave frequencies.

This paper tries to show the feasibility and validity of using an FMCW radar for remote vital sign monitoring. It compares the radar outputs with a reference sensor too. To achieve so, we will provide a signal processing flow for the measurement of the heart and breathing waveform as well as a processing scheme to estimate HR and BR. The whole analysis relies on a unique phase unwrapping process. With the help of the system model, the algorithm is explained in section II. In section III, we will introduce a mm-wave FMCW radar equipment and discuss how to choose FMCW parameters for our application. In section IV, the empirical results are discussed and in the last section,V, we will conclude the paper with some remarks and future extensions.

II. SYSTEM MODEL

Among other radars, we chose FMCW for our study. They have unique advantages, which cannot be presented in other radars at once. Those are:

- Being a mm-wave radar: the high attenuation in mm-wave frequencies provides a high isolation between the co-located operating radars even if they are separated in a few meters. Indeed, tiny displacements in mm are comparable to the wavelength thus they can be detected. This high sensitivity is required to detect the chest wall movement, which is in mm order.
- Discriminating range or localizing: because the radar can distinguish the reflections from different ranges, potentially it can be used for multi-subject vital signs detection. This feature is recognized as the main advantage of an FMCW radar in [9]. Indeed, high propagation attenuation reduces the possibility of having an echo signal, which is bounced off multiple reflectors. Most probably, the echo signal is reflected off a single object if the environment is not rich scattering. In that area,

the received signal at particular range experienced a line of sight wireless channel. In contrast, CW radars suffer from multipath fading because they collect all reflections from all objects at all visible ranges in a one sinusoid signal.

- Being robust against thermal noise: FM signals are more robust against noise in comparison to AM signals. Also, in FMCW radars the vital sign information is encoded in the received phase similar to FM signals. Thus, FMCW radar is less affected by the noise in comparison to impulse radars.

Throughout the paper, lowercase letters, boldface-lowercase letters and capital letters are used for scalars, vectors and matrixes in time domain, respectively. Boldface-capital symbols are used to represent the frequency domain variables. All vectors are column vectors. $(.)^*$ is a complex conjugate operator, and $(.)^T$ is the transpose operator. Also, estimated parameters are denoted by $\hat{(.)}$ sign. The vectors are column vectors by default otherwise it is mentioned.

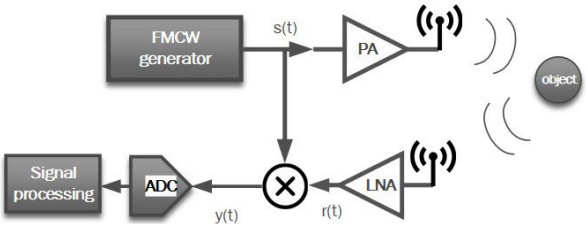

FIGURE 1. Block diagram of an FMCW radar.

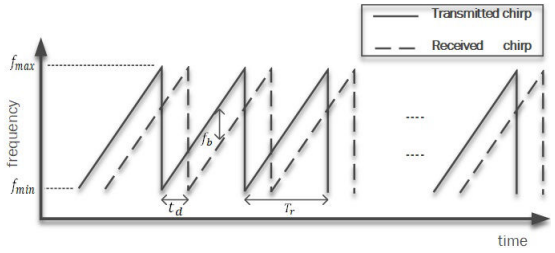

FIGURE 2. Transmitted and received chirp sequences.

A. FMCW RADAR PRINCIPLES

In any radar, the electromagnetic wave is sent into the environment containing various objects. Then the echo of the wave is captured at a receiver. A simplified block diagram of such a system is shown in Fig. 1 in which both the transmitter and the receiver are at the same location. Each chirp at the output of the FMCW generator is a sinusoid signal whose frequency is swept from f_{min} to f_{max} (Fig. 2). Here the frequency is swept linearly with a positive slope of K and a duration of T_r implying that the sweeping bandwidth is $f_{max} - f_{min} = KT_r$. The received signal at the output port of the receiver antenna is amplified and correlated with the transmit signal, which results in a signal called beat signal. The beat signal contains information about the objects in the scene. Particularly, the delay in the reflected signal is translated to an instantaneous frequency difference between the transmitted and the received chirps.

The power amplifier (PA) and the low-noise power amplifier (LNA) at the transmitter and the receiver in Fig. 1 are non-linear components. Fortunately, the FMCW signal is a constant envelop signal with the peak-to-average-power ratio (PAPR) of zero dB, which lets the amplifiers to work in their linear region. But, they adds time-varying delays to the signal even if they are in their linear operation. The time varying delay is much greater than T_r and it manifests itself as a very small Doppler shift in the baseband. This Doppler shift is in the slow-time as we will see later. In practice, the PA and the LNA delays will diminish after a while when they become thermally stable.

Assume that the complex chirp signal is:

$$s(t) = A_t \exp\left(j(2\pi f_{min} t + \pi K t^2)\right), \quad 0 < t < T_r, \quad (1)$$

f_{min} is the start frequency (and λ_{max} is the corresponding wavelength) and A_t is the magnitude related to the transmit power. Suppose that there is only a single small object situated at the distance of R_0 to the radar but it is moving around R_0, which results in a time-varying distance to the radar. Let us denote this time-varying distance by $R(t) = R_0 + x(t)$ and $x(t)$ is a function represents the distance variations around R_0. Furthermore, the reflected wave off the object at the receiver is the delayed version of $s(t)$ with a delay of $t_d = 2R(t)/c$, which is the round-trip time of the wave. c is the light speed throughout the whole paper. Consequently, the IF signal for only a single chirp duration will be:

$$\begin{aligned} y(t) &= s(t)\tilde{\mathrm{A}} - s^*(t - t_d) \\ &= A_t A_r \exp\left(j(\phi(t) - \phi(t - t_d))\right), \quad t_d < t < T_r, \end{aligned} \quad (2)$$

The thermal noise and other channel considerations are ignored for simplifications, but A_r has a relationship to A_t by the radar equation [10]. The beat signal, $y(t)$, can be expressed as follows:

$$\begin{aligned} y(t) &= A_t A_r \exp\left(j(2\pi f_{min} t_d + 2\pi K t_d t - \pi K t_d^2)\right) \\ &\approx A_t A_r \exp\left(j(2\pi f_{min} t_d + 2\pi K t_d t\right) \\ &= A_t A_r \exp\left(j(\psi(t) + \omega_b t)\right), \quad t_d < t < T_r \end{aligned} \quad (3)$$

$$y(t) \approx A_t A_r \exp\left(j(\psi(t) + \omega_b t)\right), \quad t_d < t < T_r$$

$$\psi(t) = 4\pi \frac{R_0 + x(t)}{\lambda_{max}}, \quad \omega_b = 4\pi \frac{K R_0}{c}, \quad (4)$$

the second approximate equality in (3) is obtained by ignoring the third term in the phase, which is very small. The third term is negligible because K is in $10^{12} Hz/s$ order while t_d is in $1ns$ thus the term is in the order of 10^{-6}. Equation (4) obtained after replacing t_d to (3) and ignoring the $x(t)t$ term because t is in $1\mu s$ and $x(t)$ is almost constant for one chirp as we will see later. Furthermore, $\psi(t)$ varies with $x(t)$ relative to λ_{max}. So, the phase variations in the scale of the maximum wavelength can greatly change the beat signal phase. For example, a radar operating at 6 GHz is 10 times less sensitive

in comparison to a 60 GHz radar. Thus, as a rule of thumb, the phase power for the same amount of physical displacement is 20 dB more in mm-waves. In addition, $x(t)$ is almost constant within one chirp because subjects are not moving more than 1 *mm* per chirp equivalent to $1\,mm/1\mu s = 10^3\,m/s$. Therefore, $\psi(t)$ can be approximated by sampling $x(t)$:

$$\psi(t) = 4\pi \frac{R_0 + x(t_0)}{\lambda_{max}}, \quad \omega_b = 4\pi \frac{KR_0}{c}, \tag{5}$$

where t_0 is any time in $[t_d, T_r]$. This equation is used to detect the range of a subject, R_0. To this end, an FFT is applied over samples of a chirp to obtain the spectrum of the beat signal, which has peaks corresponding to the subjects at different ranges. This FFT reveals range information so it is called range FFT. Each range FFT bin represents a particular distance with an associated phase similar to $\psi(t)$. Furthermore, as we mentioned before, there can be a very small shift in ω_b due to residual delays incurred by the PA and the LNA. Although the little frequency shift exists, it diminishes after the radar warms up.

As mentioned before, (5) does not have any information about variations of $x(t)$. To observe its variation, multiple chirps must be sent in a sequence, which is similar to the sampling of $x(t)$. Let's say that $x(t)$ is sampled each T_c, called a frame period. Therefore, $T_c \geq T_r$ and $x(t)$ appears within the phase of the range bin corresponding to the target distance (see (5)). Hence, it is possible to take a second FFT over the phase samples of that range to obtain spectral information of $x(t)$. Because it is giving vibration frequencies, thus it is a vibration FFT. In fact, $x(t)$ is a function models the chest wall displacement. As it is vibrating due to the heartbeat and exhalation or inhalation, it is a periodic function [11]. So, the spectrum of $x(t)$ contains peaks spaced equally with the fundamental frequency of the vibration, f_v. The concept behind it is that any periodic function has a Fourier series (FS) expansion with the terms, which are the harmonics of the fundamental frequency. Those harmonics appear as the peaks in the frequency spectrum.

The range of the objects and their vibration frequency, if they have a vibration, are estimated by finding ω_b in (5) and the maximum value of the range phase spectrum, $\Psi(f)$. The formulations are summarized in Table 1 with their maximum and minimum values. If there is no SNR limitation, the maximum detectable range is determined by the *Nyquist* sampling rate theorem, which sets a limit on the maximum allowable baseband frequency of f_b. The minimum range detection can be expressed as $c/2B$ where B is the sweeping bandwidth [12]. But a more practical range resolution relationship is provided in Table 1, which also considers the range FFT resolution with the size of N meaning that there are N samples in a chirp. On the other hand, the maximum frequency of vibration is related to the frame rate of $1/T_c$ at which the phase $\psi(t)$ is sampled. Similarly, the *Nyquist* sampling principle limits the maximum visible f_v as it is equated in the table. The minimum value of f_v is determined by the number of vibration FFT points, M, since the whole vibration spectrum is equally divided to M bins.

TABLE 1. FCMW radar range and velocity estimations and their min/max detectable bounds.

Parameter	Range	Vibration frequency
Estimation	$\hat{R}_0 = \frac{f_b c}{2K}$	$\hat{f}_v = \text{argmax}_f \left(\lvert\Psi(f)\rvert\right)$
Max	$\frac{cf_{b,max}}{4K}$ *	$\frac{1}{2T_c}$
Min	$\frac{cf_{b,max}}{2NK}$	$\frac{1}{MT_c}$

$*f_{b,max}$ is the sampling frequency of the ADC in Fig. 1.

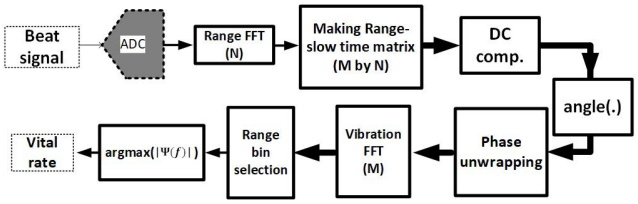

FIGURE 3. Proposed signal processing chain of the vital signs detection.

B. PROPOSED ALGORITHM

Fig. 3 shows the chronological order of the signal processing chain used for cardio-respiratory rate detection. After sampling the beat signal with $f_{b,max}$, the range FFT is applied over the samples of each chirp and the result is a vector, which is called *complex range profile*. By collecting consecutive complex range profiles from multiple chirps and putting them into a matrix in a row-wise manner, the *range-slow time matrix* is constructed with M rows (i.e. M chirps).

Prior to taking the angle of the received complex signal, one must be sure that any non-linearities, distortions, and artifacts have been removed because the phase computation is highly non-linear and it increases the complexity of removing those imperfections. For instance, the DC value of both in-phase and quadrature components of the complex signal must be removed unless otherwise, it will affect the phase quality. Suppose that the imaginary and real parts of a complex range bin are $I(t) + dc_i$, $R(t) + dc_r$, respectively. Then,

$$\phi(t) = \arctan\left(\frac{I(t) + dc_i}{R(t) + dc_r}\right) \neq \psi(t) \tag{6}$$

where dc_i, dc_r are DC values of the imaginary and real parts, respectively. In [13], they showed that the phase modulation due to the chest vibration generates so many harmonics as well as DC terms. The DC terms do not degrade the phase quality because they have inforamtion about the target displacement. In addition, [14] also discussed that the leakage between Tx and Rx can generate the DC terms. If there are DC terms due to a reason rather than the target motion, then $\phi(t)$ is not equal to $\psi(t)$ in (5). In other words, in the complex plane, the received signal constellation is shifted from the origin to $[dc_r \;\; dc_i]^T$. In Fig. 4, a constellation shift is apparent

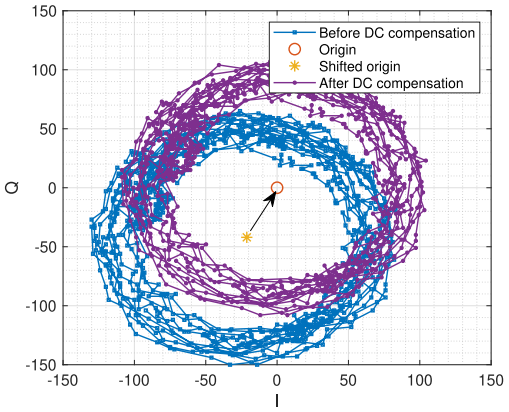

FIGURE 4. Constellation correction of the received complex signal.

in the point cloud before DC compensation. The center and the radius of the cloud can be estimated based on a non-linear least square estimation (NLLS), which is optimum in maximum liklehood (ML) sense when the noise is white Gaussian. After doing algebraic simplifications, the problem will be converted to a linear least square estimator (LLSE) as follow:

$$\boldsymbol{y}^* = \arg\min_{\boldsymbol{y}} \parallel A\boldsymbol{y} - \boldsymbol{b} \parallel^2 \tag{7}$$

where $A, \boldsymbol{b}$ are defined in the Appendix A. $\boldsymbol{y} = [R \;\; c_r \;\; c_i]^T$ is a vector of unknowns in which R is a function of the center point and the radius, and c_r, c_i are real and imaginary parts of the center point, $\boldsymbol{x}$. Fig. 4 is obtained for the actual vital signs' waveforms. Thanks to the *mm* sensitivity, the complex signal trajectory in Fig. 4 is a complete circle. This is the result of the phase dependency on the relative chest movement to the wavelength causing a great phase change only for displacements in the range of *mm*.

After DC compensation, the phase of each column in the *range-slow time matrix* is calculated by using $\tan^{-1}(.)$ so that the output phases are wrapped in $[-\pi, \pi]$. In contrast, the phase can change beyond of $\pm\pi$ because $x(t)$, the physical displacement, can be greater than $\lambda_{max}/4$ (see (5)). Therefore, there should be a mechanism to unwrap the phase beyond of $\pm\pi$. If $\psi(t)$ in (5) is sampled with an appropriate sampling time of T_c then it is possible to maintain the phase difference between two consecutive samples less than π. Equivalently, $x(t)$ must not change more than $\lambda_{max}/4$ within T_c period. If this assumption is satisfied, any phase change greater than π indicates that the phase should be corrected by adding or subtracting 2π. This process is called *phase unwrapping*, which is performed on the columns of the *range-slow time matrix* separately (Fig. 3). For a detailed analysis on the phase unwrapping process see Appendix B.

The DC value of each column is removed after *phase unwrapping* to eliminate the static clutters. Then, to find vibration frequencies, the second FFT is applied to each column resulting in a matrix contains vibrations over each range bin. This matrix is called *range-vibration map*. This map is used to search for the best range bin, which minimizes the cardio-respiratory rate estimations errors. In fact, the best range bin, or the column, is selected so that the rate estimation is the closest one to a reference sensor. We shall talk about this step of the algorithm and the reference sensor in the experiment section.

After selecting the best range, the index of the vibration frequency that has the largest magnitude and the two neighbour indexes are taken to interpolate and find a fine vibration frequency of the target. This is done by adopting Gaussian interpolation with an assumption that the spectrum over the three vibration indexes behaves analogous to a Gaussian function.

III. OUR EQUIPMENT

For our experiments, we chose a Texas Instrument (TI) mm-wave radar (AWR1443 [15]) operating from 76-81 GHz. It is a general-purpose sensor with very wide applications and it has a built-in DSP and an ARM processor for post-processing. Although the radar can run small applications stand-alone, we are not used to running our processing on the chip. In fact, after configuring the radar, the chirp samples are transferred over the UART interface to a PC to do signal analysis in Matlab. To work with the radar, an evaluation board of AWR1443 is used [16].

Using mm-wave radar is best suited for mm range displacement detection since it is desirable for the vital signs sensing. λ_{max} is 3.9 mm at 77 GHz, thus little changes of $x(t)$ in (5) can be detected. For a typical adult, the chest moves about 1-12 mm and 0.01-0.5 mm due to breathing and heartbeat respectively [17].

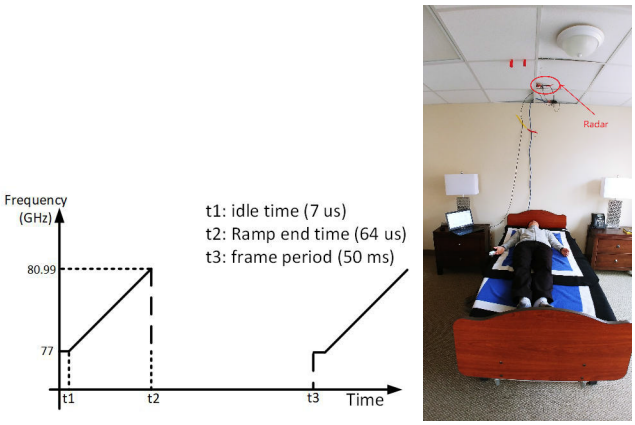

FIGURE 5. Chirp configuration (5a), and the bedroom for the tests (5b).

AWR1443 has 3 transmitters and 4 receivers, but we use a single Tx/Rx pair. The duration of each chirp is $64\mu s$ with an idle time of $7\mu s$ at the beginning of it. The idle time is required for settling the FMCW generator down when it jumps from the end frequency to the start frequency. This means that $T_r = 57\mu s$. The slope of each chirp is 70 $MHz/\mu s$ i.e. the sweeping bandwidth is 3.99 GHz. Each

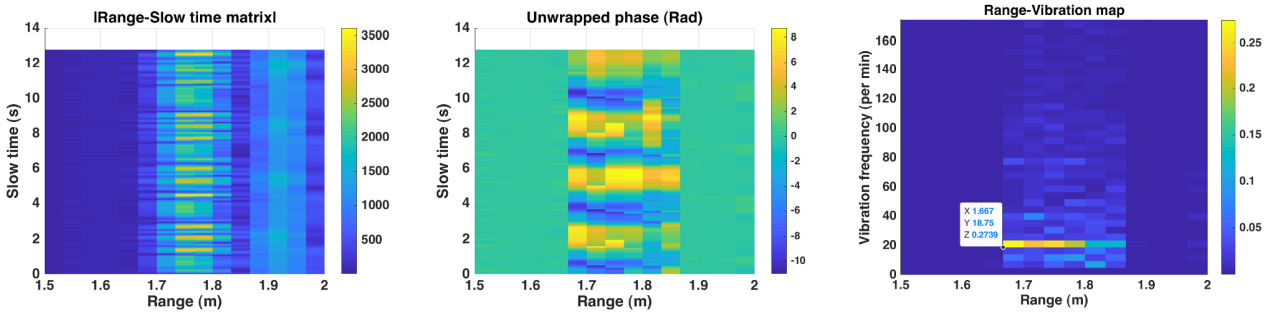

FIGURE 6. Range-slow time map (left), range-unwrapped phase map (middle), range-vibration map (right).

TABLE 2. Radar configuration parameters.

Parameter	T_r	T_c	K	$f_{b,max}$	N	M
Value	$57\mu s$	50 ms	$70MHz/\mu s$	$2MHz$	128	256

chirp is repeated every $T_c = 50\ ms$. Fig. 5 illustrates the chirp configuration used for the entire experiments. The chirp configuration along with other variables are listed in Table 2. Also with $M = 256$, the observation window for both BR and HR becomes $12.8s$. In order to increase the time resolution, half of the samples for Doppler FFT comes from the previous observation interval meaning that the observation windows are overlapped with M/2 samples. Thus, equivalently the observation duration is $6.4s$.

TABLE 3. Range and vibration frequency bounds.

Parameter	Range (m)	Vibration frequency
Max	2.14	10 Hz
Min	0.0335	0.0782 Hz

Table 3 also shows min and max allowable values of range and vibration frequency in order to detect them without ambiguity. The vibration frequency of the chest for respiration would be 0.1-0.6 Hz (or 6-36 times per minute) and that of heart rate is 0.8-2 Hz (or 48-120 beat per minute). These range of frequencies are within the acceptable vibration frequency range mentioned in Table 3.

IV. EXPERIMENTS

Fig. 5b illustrates a bedroom with a radar attached to a ceiling on the bed. A patient was lying on the bed facing up to the radar during the entire study. Indeed, a wearable device is used as a reference. This wearable sensor is a commercial product of Hexoskin, [18]. The accuracy of the sensor is examined in [19] in which the authors claimed that the device measures BR and HR for different body postures with 98% accuracy in comparison to the standard laboratory measurement tools.

A. PRIMARY RESULTS

The study was performed on a patient in a 40-minute attempt. The raw data is captured via UART port from AWR1443Boost (see [16]) to analyze offline in Matlab. At each stage of the signal processing chain, different maps are extracted. Each map conveys different information about the bedroom and vital signs and will be discussed. Finally, to complete our analysis, we will define the system performance metrics and the breathing and the heart rates' accuracies are presented.

1) THREE DIFFERENT MAPS

The raw data does not reveal any information about the environment until they are arranged and manipulated in specific forms. For instance, Fig. 6 represents three different maps obtained at different stages in Fig. 3. In all the maps, there are three different range regions:

1) Region above the bed: spanned from 1.5-1.67 m
2) Region on the body surface: spanned from 1.68-1.84 m
3) Region on the bed: spanned from 1.88-2 m

In the first region, there is no object to reflect the signal, though this is a *silent region* as it is observed in the three maps of Fig. 6.

The second region is the *body region*, which contains the reflection from different points of the body. From the radar point of view, the target is very large such that it is not a single point on the *range profile*. In fact, the two points in the space are distinctive where their distances have a difference greater than the range resolution. The range resolution, here, is 3.35 cm (see Table 3), which is enough for distinguishing the reflection from abdomen and thorax. In our study, the participant was aware of being still during the entire examination meaning that his body was moving up and down only due to cardio-respiratory activities. It is also important to notice that when we are breathing, the chest moves together with belly and even shoulders. Therefore, a large area of the body contributes to the phase modulation, thus the unwrapped phase map indicates a phase variation over multiple ranges. Among all range bins in the acceptable field of view, the best range is selected with the maximum average power. The power variation is required to distinguish the stationary clutters and

the chest modulation (Fig. 6 (left)). This is performed in the "*range bin selection*" block of Fig. 3.

In addition, it is interesting to highlight that there is somehow a constant reflection in the third region, *bed region*, which is seen as a perfect stationary clutter. The stationary clutters are eliminated after removing DC from the unwrapped phases. Therefore, the region will not have any vibration in the *range-vibration* map.

From Fig. 6 one can conclude that taking the unwrapped phase map as a base signature for vital signs monitoring has an advantage of ignoring other parts of the visible ranges by only reasoning on that whether the phase variation resembles a vital signs or it does not. However, in the maps, the only nonstationary feature is a biological activity ensuring that the range-vibration map has only frequencies of the respiration and heartbeat.[1] This assumption providing a way to achieve the main purpose of the study that is showing the validation and feasibility of using a mm-wave radar for remote vital sign sensing.

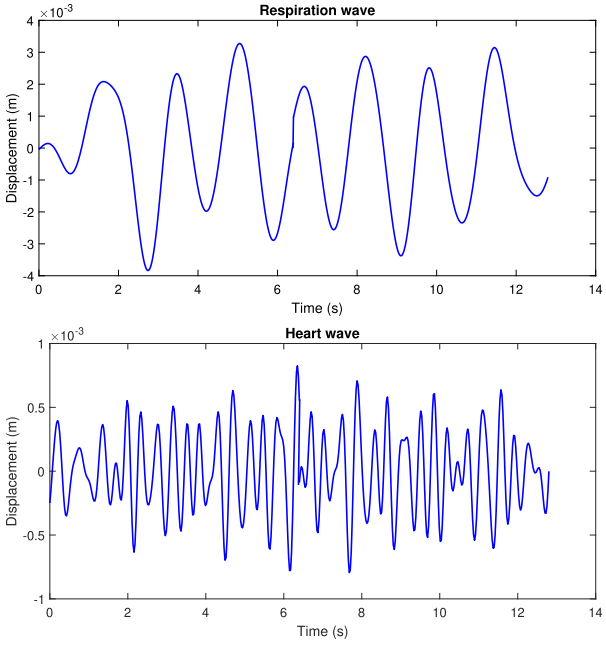

FIGURE 7. A sample of heart (bottom) and breathing (top) waveforms vs time.

2) HEART AND BREATHING WAVEFORMS

As depicted in Fig. 3, after finding the best rang bin, one can use to filter out the breathing or heartbeat frequencies of $\psi(t)$ to obtain corresponding waveforms. Each waveform in Fig. 7 is a time-variation of the chest displacement due to heartbeat or respiration. The magnitude of the breathing waveform is about 10 times of the heartbeat waveform and the later has a higher number of peaks than the former. Besides, it is possible to count the number of peaks in each waveform to obtain an estimate of the vital sign rate but that gives a poor estimation in comparison to the spectral estimation used in our proposed algorithm. Spectral estimation is optimum in maximum likelihood (ML) sense when the phase noise is Gaussian. The optimality is shown in the appendix C.

[1]For example, in the range-vibration map, there is a high peak at 18.75 bpm, which is corresponding to the BR in that moment.

B. SYSTEM PERFORMANCE

In our 40-minute trial the BR and HR are estimated based on finding the max value in their frequency range as formulated in Table 1. After removing some outliers from the estimates, which can be due to spark noises and any other external causes, the time trace along with the statistics of BR and HR are shown in Fig. 8a and Fig. 8b. In these figures, the instantaneous values of the radar and Hexoskin estimates are compared.

To have intuitions, some statistical parameters are defined to evaluate the similarity, robustness and confidentiality of the radar estimations with respect to Hexoskin estimates. If **e** is an error vector with the elements of e_i, then the standard deviation of the error can be stated as:

$$\sigma_e = \sqrt{\frac{1}{P}\sum_{i=1}^{P}(e_i - \bar{e})^2} = \| \boldsymbol{e} \|, \tag{8}$$

which is the standard deviation where $(\bar{.})$ and $\| \ . \ \|$ are the notations for statistical mean and second norm of a vector respectively and P is the number of data points. The correlation of variation (CV) is another factor represents the ratio between the standard deviation and the mean value of the data, d:

$$CV = \frac{\sigma_e}{\bar{d}} \times 100 \tag{9}$$

One useful parameter is Pearson correlation coefficient denoted as R_{icc}:

$$R_{icc} = \frac{\sum_{i=1}^{P}\left(d_{r_i} - \bar{d}_{r_i}\right)\left(d_{h_i} - \bar{d}_{h_i}\right)}{\sqrt{\sum_{i=1}^{P}\left(d_{r_i} - \bar{d}_{r_i}^2\right)\sum_{i=1}^{P}\left(d_{h_i} - \bar{d}_{h_i}^2\right)}}, \tag{10}$$

in which d_{r_i} and d_{h_i} are the i'th radar and Hexoskin estimations respectively. The value of R_{icc} is in the interval of $[-1, 1]$. The value of 1 means the two data sets are fully correlated and 0, in contrast, means they are uncorrelated. In fact, this correlation describes how two data sets are similar. All the metrics are annotated in the time trace figures of Fig. 8a and Fig. 8b.

The sample points cloud in radar-Hexoskin planes is plotted in Fig. 8a (right) and Fig. 8b (right) in which r is R_{icc}. The ideal case is when all the samples are sitting on $y = x$ line indicating that the radar data are the same as Hexoskin. In practice, the BR data follows a similar linear behavior around $y = x$ line with a slop of 1 and a 0 bias. Similarly, for HR, the linear fitted curve has a slop of 0.98 and a bias of 0. In the acceptable ranges of HR values, the linear fitted curve is very close to $y = x$ line while they can diverge for very lower or very higher invalid values. It is also good to

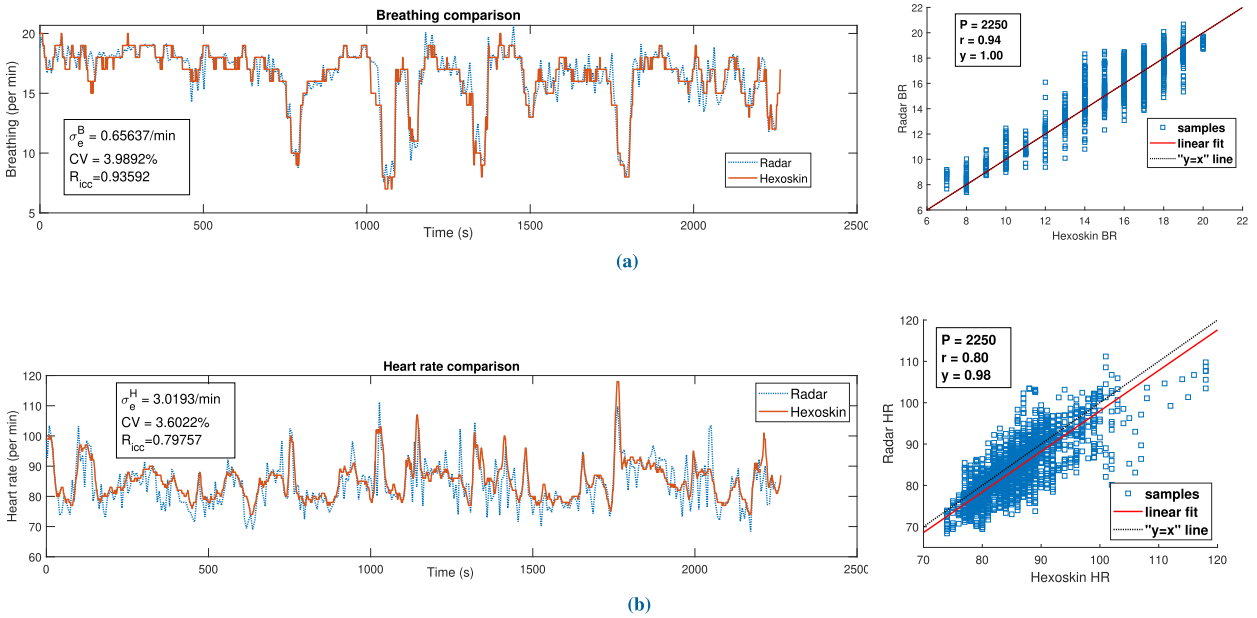

FIGURE 8. Radar BR comparison with Hexoskin (a), and radar HR comparison with Hexoskin (b). (a) BR time trace (left), radar BR vs Hexoskin BR (right). (b) HR time trace(left), radar HR vs Hexoskin HR (right).

TABLE 4. Estimation accuracy comparison to other works.

Ref.	Distance (m)	f_{min} (GHz)	HR (%)	BR (%)	p_{out} (mW)
[7]	2.48	9.6	55.2	—	25
[9]	1	80	87.2	91.08	0.5
Ours	1.7	77	80	94	15.8

mention that the BR and HR values are well distributed in the whole range of vital signs to show the agreement between the radar observation and the reference sensor.

The performance of our system is compared to the other works in Table 4. The values for the front side tests in [9] are in the table to make a fair comparison to our experiments. The performance reported in [9] has a high variance for a particular radar-target orientation. However, we consider the average performance while there might be a case the values are less than 4%. The system performance in [7] is not better than [9] and the best correct estimation rate they obtained is considered here. BR accuracy for [7] was not reported but our system shows an improvement in comparison to [9]. Our HR estimation is much more accurate than [7] and it is so close to [9]. Besides, the output power of our radar is higher than the others (last column of Table 4) but the target is somehow in a close range. Although we could not change the distance due to the space limitation in the bedroom, it is possible to use the radar for farther distances.

V. CONCLUSION

In this paper, we discussed a base theory of an FMCW radar with the phase analysis perspective. This paved the way to develop an algorithm for detecting vital signs in a realistic setting i.e. in a bedroom. In addition, operating in mm-wave has an advantage of being sensitive to a micron displacement. This feature together with FMCW radar properties motivated us to choose an mm-wave FMCW radar for our experiments. The radar tested for vital signs monitoring in a bedroom with a high agreement between the radar estimates and a reference sensor. The accuracy of the radar was compared with the other works with an improvement in the BR estimation and a close quality in HR detection. Besides, a primary application of our contribution can be a long-term monitoring of a patient who is suffering from a chronic disease such as sleep apnea. During our study, where the heartbeat waveform was shown, we realized that the radar might be used to record the ECG pattern, but it requires to increase the SNR level of the heartbeat detection in the presence of breathing. Indeed, the algorithm simply can be extended to track vital signs of multiple targets by employing the FMCW radar localization.

APPENDIX A
ESTIMATION OF THE CENTER AND THE RADIUS OF A CLOUD POINT

We want to minimize the squared error between the radius and the distance of sample points to the hypothetical center point of the cloud. Assume that we represent the complex samples as a 2D real column vectors with the first and second elements of real and imaginary parts of the complex sample, respectively. If $\boldsymbol{a}_i$ is the i'th sample point and $\boldsymbol{x}$ is the circle origin and r is the radius, then

$$\boldsymbol{a}_i = \boldsymbol{x} + r \begin{bmatrix} cos(\theta) \\ sin(\theta) \end{bmatrix} + \boldsymbol{n}_i \tag{A.1}$$

in that θ is the angle of $\boldsymbol{a}_i$ and $\boldsymbol{n}_i$ is an additive noise. If the noise is *i.i.d.*, zero-mean and Gaussian with the power of

σ_n^2, then the optimum Maximum Liklehood (ML) estimator of $\boldsymbol{x}$, r is:

$$\begin{aligned} P &= \max_{\boldsymbol{x},r} \; p_r\left(\boldsymbol{a}_i|\boldsymbol{x}, r\right) \\ &= \max_{\boldsymbol{x},r} \; \frac{1}{2\sigma_n^2} e^{-\frac{\|\boldsymbol{a}_i-\boldsymbol{x}\|^2-r^2}{2\sigma_n^2}} \\ &= \min_{\boldsymbol{x},r} \; \| \boldsymbol{a}_i - \boldsymbol{x} \|^2 - r^2 \end{aligned} \tag{A.2}$$

Consider all $\boldsymbol{a}_i$'s to minimize the squared error:

$$\begin{aligned} P &= \min_{\boldsymbol{x},r} \; \sum_{i=1}^{N} \left(\| \boldsymbol{x} - \boldsymbol{a}_i \|^2 - r^2 \right)^2 \\ &= \min_{\boldsymbol{x},r} \; \sum_{i=1}^{N} \left(\| \boldsymbol{x} \|^2 - 2\boldsymbol{a}_i^T x + \| \boldsymbol{a}_i \|^2 - r^2 \right)^2 \end{aligned} \tag{A.3}$$

N is the number of samples. The last summation resembles of the second norm of a vector. By rearranging the inner bracket terms and putting unknowns in a vector, $\boldsymbol{y}$, and knowns in a vector $\boldsymbol{b}$ the following equation can be obtained:

$$P = \min_{y} \quad \| A\boldsymbol{y} - \boldsymbol{b} \|^2 \tag{A.4}$$

$y = [R \;\; \boldsymbol{x}^T]^T$, $R = \| \boldsymbol{x} \|^2 - r^2$, and $A, \boldsymbol{b}$ are:

$$A = \begin{bmatrix} 1 & -2\boldsymbol{a}_1^T \\ 1 & -2\boldsymbol{a}_2^T \\ \vdots & \vdots \\ 1 & -2\boldsymbol{a}_N^T \end{bmatrix}, \quad \boldsymbol{b} = \begin{bmatrix} -\| a_1 \|^2 \\ -\| a_2 \|^2 \\ \vdots \\ -\| a_N \|^2 \end{bmatrix} \tag{A.5}$$

A is a full column rank matrix for $N > 3$, thus has a left inverse of $A^\dagger$ and the optimum solution is:

$$\boldsymbol{y}^* = A^\dagger \boldsymbol{b} = (A^T A)^{-1} A^T \boldsymbol{b} \tag{A.6}$$

The optimum solution of P in (A.3) is equal to the optimum solution in (A.4) when $r = \| \boldsymbol{x} \|^2 - R > 0$. By contradiction, if $r < 0$ and $\boldsymbol{y}^* = [R \; \boldsymbol{x}^T]^T$ is optimum the following shows $\boldsymbol{y}^*$ is not optimum:

$$\begin{aligned} 0 \le \| \boldsymbol{x} - \boldsymbol{a}_i \|^2 &= \| \boldsymbol{x} \|^2 - 2\boldsymbol{a}_i^T \boldsymbol{x} + \| \boldsymbol{a}_i \|^2 \\ &< R - 2\boldsymbol{a}_i^T \boldsymbol{x} + \| \boldsymbol{a}_i \|^2, \quad \forall i \end{aligned} \tag{A.7}$$

therefore each term of the summation in (A.3) with $\boldsymbol{y}^*$ is greater than when $y = [\| \boldsymbol{x} \|^2 \quad \boldsymbol{x}^T]^T$ implying that r has to be zero.

APPENDIX B
PHASE UNWRAPPING

In the signal processing, the phase of the elements in the *range-slow time* matrix is taken. The column of the resulted matrix is the phase evolution of the echo signal at a particular range. We should do the phase unwrapping on the column corresponding to our desired target range. Let's denote the phase sequence as ϕ_n for $n = 1, \cdots, M$, namely M is the size of the vibration FFT. For every pair of (ϕ_n,ϕ_{n+1}) we knew that $|\phi_{n+1} - \phi_n|$ should not be greater than π. If it is then

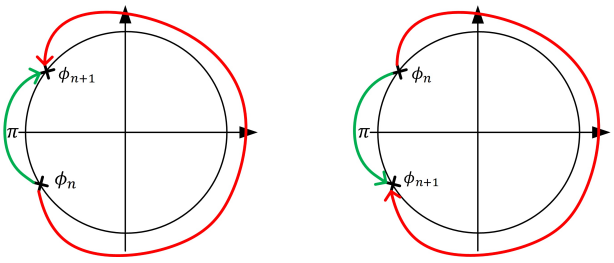

FIGURE 9. Phase jump cases: phase difference of greater than π (left), phase difference of less than $-\pi$ (right). The red lines are the unacceptable paths for phase change while the green lines are the acceptable paths.

a phase correction must be applied. The phase correction is accomplished as bellow:

- $\phi_{n+1} - \phi_n > \pi$: means that $\phi_{n+1} > 0$ and $\phi_n < 0$. As illustrated in Fig. (9, left), it seems the target followed the path shown in the red color just in T_c period. But, with our assumption it should pass the green path, which is shorter and it is less than π. To achieve so, 2π must be subtracted from ϕ_{n+1}.
- $\phi_{n+1} - \phi_n < -\pi$: means that $\phi_{n+1} < 0$ and $\phi_n > 0$. Similarly, in Fig. (9, right) it is shown that the target is followed the long path with the red color while the correct one is the shorter one. To correct, this time 2π must be added to ϕ_{n+1}.

The whole process must be done in a sequence starting with n=1 and ending with n=M-1. At each iteration, ϕ_{n+1} is only updated. The algorithm 1 explains the process.

Algorithm 1 Phase Unwrapping Procedure

r is the desired detected range index;
$\boldsymbol{r}_{desired} = R(:, r)$ (R is the *range-slow time* matrix and Matlab syntax is used to select the r'th column);
$\boldsymbol{\phi} = tan^{-1}(\boldsymbol{r}_{desired})$;
for *n=1:M-1* **do**
  if $\phi_{n+1} - \phi_n > \pi$ **then**
    $\phi_{n+1} = \phi_{n+1} - 2\pi$;
  else if $\phi_{n+1} - \phi_n < -\pi$ **then**
    $\phi_{n+1} = \phi_{n+1} + 2\pi$;
  else
    Do nothing;
end

APPENDIX C
OPTIMALITY OF FREQUENCY ESTIMATION

We can write $\psi(t)$ in discrete form by considering a noise term as follows:

$$\psi[n] = \theta_0 + \frac{4\pi}{\lambda_{max}} x[n] + w[n], \quad n = 0, 1, 2, \ldots, M-1 \tag{C.1}$$

$w[n]$ is a phase noise and $x[n]$ can be any member of $e^{j\frac{2\pi}{M}pn}$, $p = 0, 1, \cdots, M-1$ and M is the phase FFT size (see Table 1). Let $x_i[n] = e^{j\frac{2\pi}{M}in}$ for $n = 0, 1, \cdots, M-1$,

thus the problem of finding the desired vital sign frequency is to find a $x_i[n]$ such that the following will be satisfied in an interval of M samples:

$$\max_i \; p_r \left(\psi[n] \middle| x_i[n] \right) \tag{C.2}$$

in which p_r is the conditional probability. (C.2) is maximum likelihood (ML) criterion and it is optimum when all possible $x_i[n]$ can happen with equal probability and equal power. Then it can be shown that (C.2) is equivalent to the minimum Euclidean distance criterion between $\psi[n]$ and $x_i[n]$. Furthermore, if $w[n]$ can be an independent and identically distributed (i.i.d.) Gaussian random process or any other i.i.d. random process having a pdf as a function of $|x - \bar{x}|$ where x is the random process and $\bar{x}$ is its mean. Then (C.2) is equal to the following:

$$\max_i \left| \sum_{n=0}^{M-1} \psi[n] x_i^*[n] \right| = \max_i \; corr\left(\psi[n], x_i[n]\right) \tag{C.3}$$

It is enough to show that the following is true:

$$\underset{\alpha<i<\beta}{\text{argmax}} \left| \boldsymbol{\Psi}^T \boldsymbol{e}_i \right| = \underset{\alpha<i<\beta}{\text{argmax}} \; corr\left(\psi[n], e^{-j\frac{2\pi in}{M}}\right) \tag{C.4}$$

where $\boldsymbol{\Psi}$ is a vector containing positive frequency samples of the phase discrete-time Fourier transform (DFT). $\psi[n]$ is the discrete-time phase corresponding to the phase in (5), $\boldsymbol{e}_i$ is a vector having only one at the i'th position, and α, β are the frequency indexes for the desired range of frequencies. For instance, breathing frequency is in [0.1, 0.6] Hz and α, β are set to 0.1 and 0.6 Hz respectively. For proving (C.4), we start to expand the inner argument of the left-hand side of the equation:

$$\boldsymbol{\Psi}^T \boldsymbol{e}_i = DFT\left(\psi[n] \circledast e^{j\frac{2\pi n}{M} i}\right) \tag{C.5}$$

$$= DFT\left(\sum_{l=0}^{M-1} \psi[l] e^{j\frac{2\pi i}{M}(n-l)}\right) \tag{C.6}$$

$$= \frac{1}{M} \sum_{n=0}^{M-1} \left[\sum_{l=0}^{M-1} \psi[l] e^{j\frac{2\pi i}{M}(n-l)} \right] e^{-j\frac{2\pi}{M} nk} \tag{C.7}$$

$$= \sum_{l=0}^{M-1} \psi[l] e^{-j\frac{2\pi}{M} il} \sum_{n=0}^{M-1} \frac{1}{M} e^{-j\frac{2\pi n}{M}(i-k)} \tag{C.8}$$

$\circledast$ is a circular convolution is used to convert frequency multiplication to time-domain convolution. In (C.7) k is the index of FFT and l is the index of convolution. After interchanging the summation orders in (C.7), (C.8) is obtained in which the second summation is $\delta(i - k)$. By replacing it in (C.8), (C.4) is proved.

ACKNOWLEDGMENT

This research is conducted with the approval of office of research ethics (ORE) in the University of Waterloo. And the ORE reference number is 22770. Also thank to Dr. Doojin Lee for his help in collecting experimental data.

REFERENCES

[1] M. Vespe, G. Jones, and C. J. Baker, "Lessons for radar," *IEEE Signal Process. Mag.*, vol. 26, no. 1, pp. 65–75, Jan. 2009.
[2] N. Du, K. Liu, L. Ge, and J. Zhang, "ApneaRadar: A 24 GHz radar-based contactless sleep apnea detection system," in *Proc. 2nd Int. Conf. Frontiers Sensors Technol. (ICFST)*, Apr. 2017, pp. 372–376.
[3] S. M. A. T. Hosseini and H. Amindavar, "UWB radar signal processing in measurement of heartbeat features," in *Proc. IEEE Int. Conf. Acoust., Speech Signal Process. (ICASSP)*, Mar. 2017, pp. 1004–1007.
[4] S. Ayhan, S. Scherr, A. Bhutani, B. Fischbach, M. Pauli, and T. Zwick, "Impact of frequency ramp nonlinearity, phase noise, and SNR on FMCW radar accuracy," *IEEE Trans. Microw. Theory Techn.*, vol. 64, no. 10, pp. 3290–3301, Oct. 2016.
[5] M. C. Budge and M. P. Burt, "Range correlation effects in radars," in *Proc. Rec. IEEE Nat. Radar Conf.*, Apr. 1993, pp. 212–216.
[6] Ø. Aardal, Y. Paichard, S. Brovoll, T. Berger, T. S. Lande, and S.-E. Hamran, "Physical working principles of medical radar," *IEEE Trans. Biomed. Eng.*, vol. 60, no. 4, pp. 1142–1149, Apr. 2013.
[7] L. Anitori, A. de Jong, and F. Nennie, "FMCW radar for life-sign detection," in *Proc. IEEE Radar Conf.*, May 2009, pp. 1–6.
[8] C. Li, V. M. Lubecke, O. Boric-Lubecke, and J. Lin, "A review on recent advances in Doppler radar sensors for noncontact healthcare monitoring," *IEEE Trans. Microw. Theory Techn.*, vol. 61, no. 5, pp. 2046–2060, May 2013.
[9] S. Wang *et al.*, "A novel ultra-wideband 80 GHz FMCW radar system for contactless monitoring of vital signs," in *Proc. IEEE 37th Annu. Int. Conf. Eng. Med. Biol. Soc. (EMBC)*, Aug. 2015, pp. 4978–4981.
[10] C. A. Balanis, *Modern Antenna Handbook*. Hoboken, NJ, USA: Wiley, 2008.
[11] L. Ding, M. Ali, S. Patole, and A. Dabak, "Vibration parameter estimation using FMCW radar," in *Proc. IEEE Int. Conf. Acoust., Speech Signal Process. (ICASSP)*, Mar. 2016, pp. 2224–2228.
[12] P. Pahl, T. Kayser, M. Pauli, and T. Zwick, "Evaluation of a high accuracy range detection algorithm for FMCW/phase radar systems," in *Proc. 7th Eur. Radar Conf.*, Sep./Oct. 2010, pp. 160–163.
[13] C. Li and J. Lin, "Random body movement cancellation in Doppler radar vital sign detection," *IEEE Trans. Microw. Theory Techn.*, vol. 56, no. 12, pp. 3143–3152, Dec. 2008.
[14] F. Zhu, K. Wang, and K. Wu, "A fundamental-and-harmonic dual-frequency Doppler radar system for vital signs detection enabling radar movement self-cancellation," *IEEE Trans. Microw. Theory Techn.*, vol. 66, no. 11, pp. 5106–5118, Nov. 2018.
[15] *AWR1443 Single-Chip 76-GHz to 81-GHz Automotive Radar Sensor Integrating MCU and Hardware Accelerator | TI.com*. [Online]. Available: http://www.ti.com/product/AWR1443
[16] *AWR1443 Single-Chip 76-GHz to 81-GHz Automotive Radar Sensor Evaluation Module | TI.com*. [Online]. Available: http://www.ti.com/tool/AWR1443BOOST
[17] A. D. Droitcour, "Non-contact measurement of heart and respiration rates with single chip microwave Doppler radar," Ph.D. dissertation, Stanford Univ., Stanford, CA, USA, 2006.
[18] Carre Technologies Inc (Hexoskin). *Hexoskin Smart Shirts—Cardiac, Respiratory, Sleep & Activity Metrics*. Accessed: Apr. 27, 2019. [Online]. Available: https://www.hexoskin.com/
[19] R. Villar, T. Beltrame, and R. L. Hughson, "Validation of the hexoskin wearable vest during lying, sitting, standing, and walking activities," *Appl. Physiol., Nutrition, Metabolism*, vol. 40, no. 10, pp. 1019–1024, 2015.

MOSTAFA ALIZADEH received the two B.S. degrees in electrical and computer engineering in the sub-fields of electronics and communications and the M.Sc. degree in electrical and computer engineering and wireless communications from the Amirkabir University of Technology (Tehran's Polytechnic), in 2012 and in 2014, respectively. He attended to University of Waterloo as a Ph.D. student in Fall 2016. His current research interests include signal processing and implementation with more interests in biomedical signal processing, radar and sensor analysis, MIMO radars, RF system design, and electromagnetic engineering.

GEORGE SHAKER received the B.A.Sc., M.A.Sc., Ph.D. degrees.

He has been an Adjunct Assistant Professor with the Department of Electrical and Computer Engineering, University of Waterloo, since 2014. He is also with Sparktech Labs., (formerly DBJay Ltd.,), where he has been the Principal Scientist and the Head of Electromagnetics Research and Development, since 2011. From 2011 to 2013, he was a Senior Team Member and the Head of Technology of DBJ's Sister Company in China. He was heavily involved in designing a line of compact chambers product and the line of compact chambers for next-generation wireless systems, including MIMO and RFIDs. From 2006 to 2011, he was affiliated with RIM's (Blackberry's) RF Research and Development Division, first as an NSERC Scholar, then as a Senior EM Researcher, reporting directly to the RIM's Vice President of RF Research and Development. From 2009 to 2010, he was a Visiting NSERC MSFSS Scholar with the Georgia Institute of Technology. Over the last decades, he has contributed to products available from Hi-Tek International, Panasonic, ActsPower, COM DEV Ltd., Research in Motion (BlackBerry), American Microelectronic Semiconductors (ON-Semiconductors), Bionym, Medella Health, Novela, DBJ Tech, Konka, Enice, China Mobile, Tri-L Solutions, Pebble, Thalmic Labs, Lyngsoe Systems, NERV, and Spark Tech Labs. He has coauthored two papers in the IEEE Sensors, which were among the top 25 downloaded papers on the IEEEXplore for several consecutive months, in 2012 and 2017. He has also coauthored over 70 journal publications, conference papers, and technical reports, along with more than 15 patents/patent applications. He has served as a TPC/TPRC Member of the IEEE MTT-IMS, the IEEE iWAT, the IEEE EMC, the IEEE WF-IoT, the IEEE AP-S, the IEEE EuCAP, and the IEEE iThings. He was an Invited Speaker with several international events, including Keynote talks at the IEEE LAPC, the IEEE iThings, and the Ambient Intelligence.

Dr. Shaker was a recipient of multiple awards, including the NSERC Canada Graduate Scholarship (sole winner in the area of electromagnetics across Canada, in 2007), the Ontario Graduate Scholarship (twice), the European School of Antennas Grant at IMST GmbH, in 2007, the top 3 IEEE AP-S Best Paper Award, in 2009, the IEEE AP-S Best Paper Award (HM, in 2008, 2011, and 2017), the IEEE Antennas and Propagation Graduate Research Award, from 2008 to 2009, the NSERC CGS-FSS, in 2009, the IEEE MTT-S Graduate Fellowship, in 2009, the Electronic Components and Technology Best of Session Paper Award, in 2010, the Google Soli Alpha, in 2015, and the IEEE AP-S Third Best Student Design Award, in 2016. He has served as the Session Co-Chair and Short Course/Workshop Lecturer in several international scientific conferences. He currently serves as an Associate Editor for the *IET Microwaves, Antennas, and Propagation*.

JOÃO CARLOS MARTINS DE ALMEIDA is currently pursuing the Ph.D. degree in electrical engineering with the School of Electrical and Computer Engineering, University of Campinas, in Brazil. He was also a Visiting Graduate Student with the Ubiquitous Health Technology Lab, University of Waterloo. He has been involved in multidisciplinary teams in the development and testing of medical devices for minimally invasively detecting health conditions, allowing better patient care.

PLINIO PELEGRINI MORITA is currently an Assistant Professor with the School of Public Health and Health Systems, University of Waterloo. He is the J. W. Graham Information Technology Emerging Leader Chair of applied health informatics. He is currently with the University Health Network, the University of Toronto, and the Research Institute for Aging. As the Director of the Ubiquitous Health Technology Lab (UbiLab), he has focused his research on population level surveillance, remote patient monitoring (RPM), and personalized medicine technologies to be used to prevent unnecessary visits to hospitals and drive our healthcare system toward community care and telehealth. The UbiLab expands the area of population-level surveillance, remote patient monitoring, and precision medicine by developing algorithms and the systems of systems that combine data from mHealth and the IoT sensor technology that can satisfy clinical standards while also providing meaningful use for the patient to the ocean of data currently collected by these smart technologies.

SAFEDDIN SAFAVI-NAEINI was born in Gachsaran, Iran, in 1951. He received the B.Sc. degree in electrical engineering from the University of Tehran, Tehran, Iran, in 1974, and the M.Sc. and Ph.D. degrees in electrical engineering from the University of Illinois, Urbana–Champaign, in 1975 and 1979, respectively. He joined the Department of Electrical and Computer Engineering, University of Tehran, as an Assistant Professor, in 1980, where he became an Associate Professor, in 1988. In 1996, he joined the Department of Electrical and Computer Engineering, University of Waterloo, ON, Canada, where he is currently a Full Professor and the RIM/NSERC Industrial Research Chair of intelligent radio/antenna and photonics. He is also the Director of a newly established Center for Intelligent Antenna and Radio System (CIARS). He has published over 80 journal papers and 200 conference papers in international conferences. His research activities deal with RF/microwave technologies, smart integrated antennas and radio systems, mmW/THz integrated technologies, nano-EM and photonics, EM in health sciences and pharmaceutical engineering, antenna, wireless communications and sensor systems and networks, new EM materials, bio-electro-magnetics, and computational methods. He has led several international collaborative research programs with research institutes in Germany, Finland, Japan, China, Sweden, and USA.